CrossMark

ORIGINAL ARTICLE

Diode area melting single-layer parametric analysis of 316L stainless steel powder

Miguel Zavala-Arredondo[1] · Kristian M. Groom[2] · Kamran Mumtaz[1]

Abstract Diode area melting (DAM) is a novel additive manufacturing process that utilises customised architectural arrays of low power laser diode emitters for high speed parallel processing of metallic powdered feedstock. The laser diodes operate at shorter laser wavelengths (808 nm) than conventional SLM fibre lasers (1064 nm) theoretically enabling more efficient energy absorption for specific materials. This investigation presents a parametric analysis of the DAM process, identifying the effect of powder characteristics, laser beam profile, laser power and scan speed on the porosity of a single-layer sample. Also presented is the effect of process energy density on melt pool depth (irradiated thermal energy penetration capable of achieving melting) on 316L stainless steel powder. An analysis of the density and the melt depth fraction of single layers is presented in order to identify the conditions that lead to the fabrication of fully dense DAM parts. Energy densities in excess of 86 J/mm^3 were theorised as sufficient to enable processing of fully dense layers.

Keywords Selective laser melting · Diode area melting · Additive manufacturing · Laser diode · Advanced manufacturing, high speed

✉ Kamran Mumtaz
k.mumtaz@sheffield.ac.uk

1 Department of Mechanical Engineering, University of Sheffield, Sheffield S1 3JD, UK

2 Department of Electronic & Electrical Engineering, University of Sheffield, Sheffield S1 3JD, UK

1 Background

Additive manufacturing (AM) is a disruptive viable alternative to conventional manufacturing processes, capable of creating geometrically efficient structures with low material wastage. Laser-based selective laser melting (SLM) and electron-based electron beam melting (EBM) AM systems are increasingly being used in high value sectors to directly manufacture metallic end-use parts from a variety of alloys. During processing, the melting source (deflected laser/ electron beam) selectively scans and melts regions of a pre-deposited powder bed. Cross-sections of the part are fused in layers, built up successively to create the complete 3D object. This method of layered fabrication, combined with the high precision of laser melting allows for a greatly expanded design freedom with minimal feedstock waste.

1.1 Metallic powder bed additive manufacturing technologies

SLM or EBM are considered direct AM processes, capable of fully melting powdered feedstock with the ability to process a variety of metals to near full density. SLM typically uses a galvo scanning mirror to mechanically deflect a single fibre laser spot (continuous wave or modulated, operating at a laser wavelength of 1.06 μm) over a powder bed along a path that corresponds to the cross-sectional geometry of the component that is being formed [1]. This process is repeated layer upon layer until the part has been fully formed. This method of scanning from a single laser source and its reliance on mechanical galvo scanning limits the processing speed of the system. The process can only manufacture as quickly as the laser can be deflected whilst maintaining a sufficiently high energy density to achieve melting. SLM system manufacturers have attempted to increase system productivity through

🙌 Springer

an increase in laser power (500–1000 W) so that sufficiently high energy densities are achieved as the galvo mirrors deflect the laser beam at much higher speeds. SLM system manufacturers have also introduced new products that integrate multiple parallel fibre lasers into a single system. The lasers simultaneously scan a powder bed, effectively increasing volumetric build rate. However, there are practical space limitations when integrating multiple fibre lasers into a single system (each requiring its own cooling, optics train/galvo mirror, etc.). Further to this, the cost of the overall system significantly increases when integrating further lasers, as does its power consumption. Miller et al. have demonstrated this parallel beam approach for a high-power, multi-beam laser processing system that comprises multiple independent pairs of selectively rotatable galvo mirrors [2]. However, this approach substantially increases equipment cost and energy consumption, with scanning speed still limited by mechanical movement of the multiple galvo systems. Furthermore, as the laser spot travels from the centre of the focusing optic during scanning, the beam profile deteriorates and power is reduced. There are therefore limits to the area a single deflected laser source can reliably melt.

The EBM process uses the same building principal as SLM, but instead of a fibre laser it uses a high-power electron gun (up to 3.5 kW), deflected via magnetism to melt powdered feedstock [3]. The electron gun can be deflected faster than a galvo mirror (electron spot capable of travelling up to 8000 m/s), has a higher power than SLM systems and its electron beam can be split into multiple spots allowing a much faster build rate than SLM (80 cm^3/h EBM compared to 5–20 cm^3/h SLM). However, this speed comes at a cost, with the methodology and apparatus used within EBM systems being generally more expensive than SLM systems, limiting its industrial uptake. Furthermore, the surface finish is generally of a poorer quality in EBM, and the systems are also known to be more temperamental due to the use of an electron beam melting source.

1.2 Direct applications of laser diodes for high speed AM processes

High-power diode lasers (HPDL) are used in direct material processing applications such as surface treatments, soldering, welding and cutting. Their advantages include compactness, energy efficiency, lifetime and running costs compared to conventional material processing lasers such as fibre, Nd:YAG or CO_2 lasers [4]. However, HPDLs suffer very high beam divergence and each single laser diode emitter within a bar array still individually emits a relatively low power (< 5 W compared to > 200 W of fibre, Nd:YAG or CO_2 lasers). This has led to the popular belief that the direct application of laser diodes in AM processes is limited. Fraunhofer ILT have developed a new HPDL-based multi-spot SLM system capable

of achieving 200 W power per melting spot, comparable to SLM. In order for such a high-power laser spot to be achieved, multiple laser diode bars are required to be stacked/combined with multiple emitters multiplexed to create each of the single 200 W laser spots [5] [6]. No details have been reported on how many laser multi-spots have been integrated into this new Fraunhofer machine, nor has information been disclosed detailing its processing performance or quality of produced samples. Matthews et al. recently demonstrated a diode-based additive manufacturing (DiAM) system [7]. The laser diode sources used within the DiAM method are comprised of a set of four 1.25 kW continuous wave (CW) stacked diode arrays (60 individual bars each) giving a total of 4.8 kW power from a combined incoherent beam at 150 A. An optically addressable photomask captures the incoherent light in order to selectively melt a maximum single shot area of 2–3 mm with a ~ 10-mm-wide hybrid laser beam composed of the diode laser beams together with a Q-switched Nd:YAG laser beam. The maximum practical area of the DiAM system is limited by the short pulse laser which produces a non-uniform Gaussian intensity profile with only the central 2–3 mm of the laser beam being sufficiently uniform. The capabilities of DiAM have been demonstrated with low melting temperature Sn powder. However, part density has not been reported and high temperature engineering metallic materials (i.e. stainless steel) have not been analysed.

Diode area melting (DAM) is a novel powder-based AM process for the manufacture of metallic components [8]. The DAM methodology replaces the traditional galvo scanning methodology used within a single fibre laser SLM system with multiple non-deflected low power laser diode beams that scan and selectively melt powdered feedstock material in parallel. The ability to process materials with melt temperatures in excess of 1400 °C using DAM has been demonstrated by Zavala-Arredondo et al. [8]. A multi-layer stainless steel sample with areas of cross-sectional micro density comparable to SLM has been reported.

Within the work presented by Zavala-Arredondo et al., a number of processing challenges were introduced which manifested from limitations of the DAM system when processing high temperature materials (i.e. stainless steel). These include the following: (1) large melting spot diameter for individual beams, with a minimum of 250 μm DAM single-spot diameter demonstrated, compared to a typical SLM spot diameter ~ 70 μm. This limits the process' resolution and restricts the maximum energy density at a given laser power and scanning velocity; and (2) non-uniform thick powder layer deposition (> 150 μm) due to the use of a manual powder deposition methodology. These two factors limit inter-layer bonding across specific areas of the sample leading to low density of the 3D part in specific and often random locations. Also experienced was a lack of substrate bonding, this may result from the thick layer deposition and limited energy density

generated. These system limitations should be overcome in order to further optimise the DAM system/process and create 3D components with consistently high density (> 99%).

2 Diode area melting and laser beam profiles

The DAM laser beam delivery system consists of fast axis collimator (FAC) and slow axis collimator (SAC) micro-lenses for beam collimation, and two plano-convex cylindrical lenses for fast and slow axis focusing [8]. The laser module used in DAM is a 50-W multi-mode edge-emitting diode laser bar array featuring 19×2.63 W emitters. The full width half maximum (FWHM) divergences of the fast and slow axis before collimation are $\theta_{\perp FWHM} = 27°$ and $\theta_{\parallel FWHM} = 7°$, respectively. After collimation, the full width divergences at the $1/e^2$-level for the fast and slow axis are $\theta_{\perp FW1/e}^2 = 0.1°$ and $\theta_{\parallel FW1/e}^2 = 2.7°$, respectively. The dimensions of the module are 10 mm bar width, 500 μm emitter spacing, 135 μm emitter width and 27% fill factor.

In DAM, individual emitters within the array are switched on/off as the lasers traverse the powder bed in order to process net-shaped parts. This requires a customised packaged module as described in work undertaken by Zavala-Arredondo et al. [8]. In this study, commercial CS-mounted bars were utilised where emitters in the array were connected together such that a continuous line array of focussed laser beams was obtained. Three different laser beam profiles (LBPs) are used in the present work to investigate the effect of melting area dimension, melting beam shape (line or multi-spot shape) and melting spot spacing. For all LBPs, emitters of the array can be switched on/off as they traverse the powder bed to create a shape. The multiple laser diode beams used in DAM to selectively melt a powder bed and build a 3D part are schematically presented in Fig. 1. From Fig. 1, The cooling system limits the laser diode temperature to the operational temperature; collimating micro-lenses (FAC and SAC) and focusing lenses (cylindrical plano-convex) control the beam path by the collimation and focusing of the laser beams; the distance, d, controls the resultant LBP used ($d = 25$ mm, $d = 30$ mm and $d = 35$ mm for LBP1, LBP2 and LBP3, respectively; see Fig. 2); the linear movement of the processing table results in the melted area from a single pass of the non-deflected beams.

The different LBPs used are depicted in Fig. 2. The total melting areas of the different LBPs are approximated as rectangles of varying dimensions for simplicity, as shown in Fig. 2. The dimensions of such areas are dependent on the single-spot mean dimensions and the spot spacing (spot period) measured as described by Zavala-Arredondo et al. [8]. The single-spot dimensions, spot spacing, total melting area and beam shape distribution of the different LBPs are shown in Table 1.
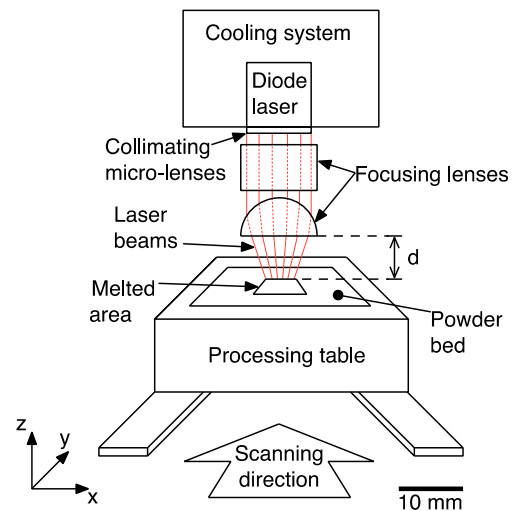

Fig. 1 Diode area melting, individually controllable emitters selectively turn on/off to melt shape over powder bed. Only the laser diode module and the melting area are scaled for visualisation

3 Experimental methodology

The DAM system is enclosed within a custom-built chamber which is purged with argon gas to reduce the oxygen concentration in the chamber to < 1000 ppm before processing. In the present embodiment, the thermoelectrically cooled laser diode module remains stationary during processing whilst the powder bed is traversed below the fixed laser. An inert gas air knife (supplying Ar) passes just above the processing table to prevent spattered contaminants from reaching the focusing optics or laser facets. A motorised bed processing table (controlled by LabVIEW), adjustable in the x and z axis, is positioned below the focusing optics at a distance, d. Single, thick 260 μm layers (deposited using a 260-μm-thick metallic mask frame on the substrate and a manually operated sliding wiper) of 316L stainless steel powder were DAM processed in order to investigate the effect of process parameters under the assumption of minimum heat dissipation of the laser-irradiated surface of the powder bed through the solid substrate. The powder bed was scanned and melted in a single pass along a 5 mm length by the laser diode module using the different LBPs described in Section 2. Two different 316L stainless steel powder particle sizes (sourced by LPW) of PD1 = 15–45 μm and PD2 = 44–106 μm (see Fig. 3) were used in order to investigate the effect of particle size distribution in the DAM process over a range of scanning velocities and laser powers.

The parameters used in the present investigation are presented in Table 2. The scan speeds selected are limited by the slow motorised stage used and by the low power and large individual melting spots that the current DAM system is capable of achieving (requiring slow scan speeds to reach energy densities high enough to melt the stainless steel powder). However, higher individual laser power densities could be achieved by using more powerful laser diode modules, using
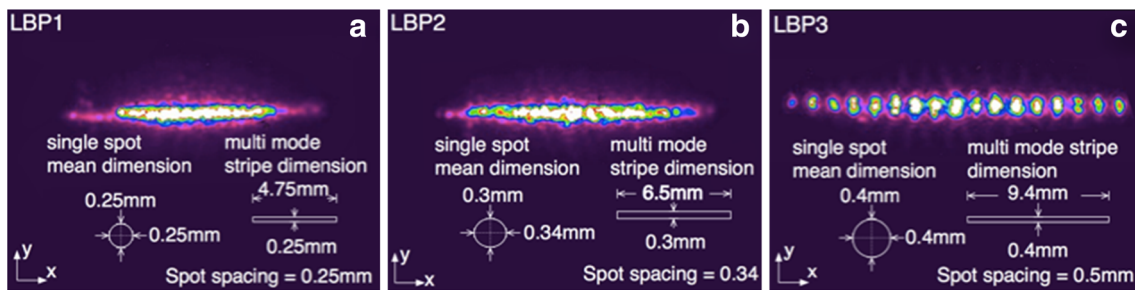
Fig. 2 Beam profiles measured using a Spiricon camera-based beam profiler and BeamMic software. Laser beam profiles **a** LBP1; **b** LBP2 and **c** LBP3 featuring different beam distributions of a (a) tight single-line, (b) large single-line and (c) individual multi-spot shapes

multiple HPDL modules multiplexed to increase power, and/or optimising the beam delivery system. Such system optimisation may allow the use of higher scanning velocities. Additionally, the process has the potential to stack multiple laser diode bars or modules across the scanning direction in order to scan the entire process layer in a single pass.

A three-level full factorial design with four replicates has been developed for each of the different particle sizes PD1 and PD2. The properties to be examined are top surface open porosity of samples and melt pool depth. Selected samples featuring < 10% top surface porosity were cross-sectioned and polished in order to analyse the cross-sectional micro/macro porosities. The samples were produced by a single scan of the different laser beam profiles (LBPs) along a 5-mm length.

For measurement of top surface open porosity, the samples were manually removed from the powder bed, cleaned and analysed using SEM. The cross-sectional thickness was measured at multiple points along the samples and a mean thickness was calculated for each sample. The thickness of the solidified part is considered to be related to the melt depth. To measure the cross-sectional porosity, selected samples featuring < 10% top surface porosity were hot mounted on Bakelite and polished for optical analysis. The mean cross-sectional micro porosity (cross-micro porosity) and the total cross-sectional macro porosity (cross-macro porosity) were measured via image processing of the optical analysis.

4 Results and discussion

Figure 4 depicts the regions or combination of parameters that resulted in bonded (i.e. successfully built) and insufficiently bonded (i.e. failed) samples for PD1 and PD2. The bonded or successfully built samples were removed from the bed to measure part's porosity and melt depth. The insufficiently bonded or failed samples resulted either in insufficient melting or weak samples that broke when lifted from the bed.

Tables 3, 4, 5 and 6 show top-view SEM images of successfully built samples for all of the different processing parameters studied. Tables 3, 4 and 5 show the PD1 samples for the laser beam profiles LBP1, LBP2 and LBP3, respectively. Table 6 shows the successfully built PD2 samples for LBP1, LBP2 and LBP3, respectively. It can be seen that the top surface open porosity of the part is highly dependent on the energy density and particle size distribution. The samples surface exhibits a more evident open porosity at lower laser powers and higher scanning velocities. This is analysed and quantified in Section 4.3. The number of failed samples (i.e. particles not fused and samples unable to be lifted/removed from the bed with tweezers) increased with decreasing energy density and increased particle size distribution of the powder feedstock. It is observed in Fig. 4 that PD2 samples had a limited number of regions (i.e. combination of parameters) that promoted successful bonding. This can be explained in terms of the limited efficiency of the laser-induced heat distribution promoted by the characteristics and larger particle sizes of PD2 (further analysed in Section 4.1). It can be seen that a higher energy density is preferable in all cases to improve the quality and consistency of the melted region.

### 4.1 Effect of particle size distribution

4.1.1 Emissivity and conductivity of powder

Powder size and morphology are important for determining the optical and thermal properties of a powder bed, such as

Table 1 Characteristics of the different laser beam profiles

Laser beam profile	Mean single-spot radii (mm)	Spot spacing (mm)	Melting area (mm²)	Melting beam dimensions (beam distribution)
LBP1	0.25 × 0.25	0.25	1.19	4.75 × 0.25 mm (stripe)
LBP2	0.3 × 0.34	0.34	1.95	6.5 × 0.3 mm (stripe)
LBP3	0.4 × 0.4	0.5	3.76	9.4 × 0.4 mm (spots)

Fig. 3 SEM images of the 316L stainless steel powders. Particle size distribution: **a** PD1 = 15–45 μm; **b** PD2 = 44–106 μm
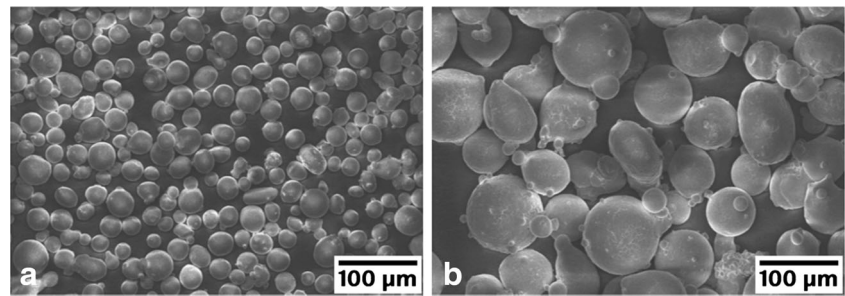
emissivity and thermal conductivity. In the case of metallic powders, the material can be considered as a grey body which means that no transmission of radiation takes place during laser irradiation. This in turn leads to the assumption that the absorptivity, α, and emissivity, ε, of a metallic particle can be considered to be equal ($\alpha = \varepsilon$). However, a powder bed cannot be considered as a bulk solid material due to the large amount of porosity caused by the existing cavities between particles. The total volume of such cavities is dependent on the particle size and morphology. The material of interest can be considered to have regular spherical morphology with a range of particle diameters (Fig. 3). However, Fig. 3b shows the presence of satellite defects adjacent to the PD2 larger particles. The emissivity of a powder bed during laser radiation can be assumed to be caused by the emission of the cavities and the emission of the heated metallic particles. The emissivity and conductivity of the PD1 and PD2 powders (shown in Fig. 5) were calculated using the Sih and Barlow method [9]. Table 7 shows the properties of the powders used in calculation of emissivity and conductivity. A difference of 1% in fractional porosity, φ_f, between PD1 and PD2 powders provides negligible difference in the emissivity of the powder beds (see Fig. 5a). However, the PD1 powder showed a significantly higher conductivity than that of PD2 as demonstrated in Fig. 5b, due to the higher fractional packing density caused by the smaller particle size distribution. This characteristic may play an important role when processing at low individual laser powers used in DAM.

4.1.2 Effect of powder bed characteristics on response trends

Figure 6a plots the top surface porosity as a function of energy density for PD1 and PD2. The top surface porosity is observed

to reduce logarithmically with increasing energy density. The data points in Fig. 6 represent all the successfully built (i.e. fused together) parts. It can be seen that the number of successfully built samples is significantly higher for PD1. It can also be seen that a larger number of PD1 samples have < 10% porosity compared to PD2. This can be explained in terms of the higher efficiency of thermal distribution for PD1 powder due to its higher conductivity (as observed in Fig. 5b). The higher conductivity resulted in a more uniform temperature distribution induced at higher energy densities. Large particle diameters lead to decreased packing densities, which limit thermal conductivity and restrict the densification of the melt promoting the formation of pores. Reducing the particle size distribution (i.e. PD2 to PD1) will lead to a decreased top surface porosity, similar in proportion to the increase in conductivity observed in Fig. 5b. Therefore, it is considered that the conductivity of the powder (governed by the packing
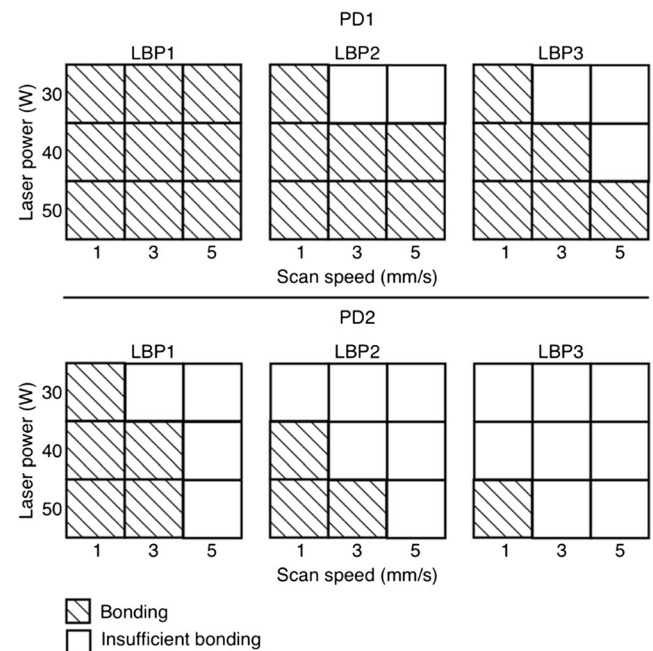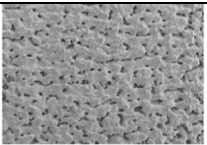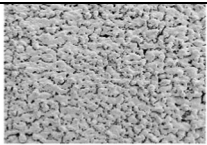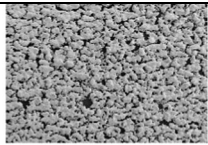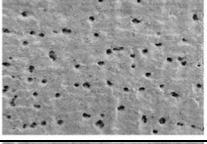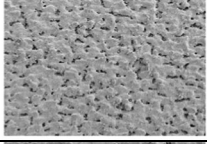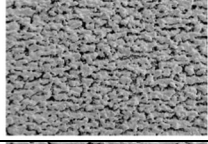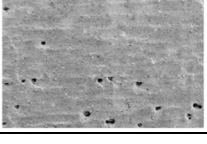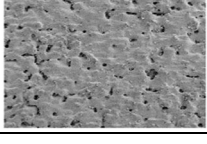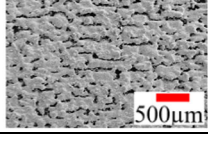

Fig. 4 Regions (i.e. combination of parameters) showing bonding and insufficient bonding for PD1 and PD2 samples. Bonding regions resulted in samples that could be lifted from the bed for porosity and melt depth analysis. Regions of insufficient bonding (i.e. failed samples) resulted in either non-melted samples or weak samples that broke when lifted from the bed, preventing from further porosity/melt depth analysis

Table 2 Process parameters used for the single-layer parametric investigation of 316L stainless steel

Powder particle diameter range	PD1 = 15–45 μm and PD2 = 44–106 μm
Laser beam profile[a]	LBP1, LBP2 and LBP3
Scanning velocities	1, 3 and 5 mm/s
Laser power	30, 40 and 50 W

[a] See Table 1

Table 3 SEM images of the top view of PD1-LBP1 samples

LBP1		
|← 4.75 mm →|		
Scan speed / **Laser power**	1 mm/s	3 mm/s	5 mm/s

	1 mm/s	3 mm/s	5 mm/s
30 W			
40 W			
50 W			500μm

density of the powder bed) and the top surface porosity are directly correlated. The measured melt depths of samples are plotted as a function of energy density in Fig. 6b. For both PD1 and PD2, melt depth increases with increasing energy density before saturating at high energy densities. It can be seen that PD2 showed higher melt depth even though it presented the highest porosity. This suggests that the PD2 size resulted in thick, highly porous samples being produced whilst the densely packed PD1 resulted in denser, thinner samples. The large melt depth measured in PD2 samples may be due to the formation of large balls (balling) and lumps of melted powder with weak bonding necks and partially fused particles. Such balling resulted in thicker samples (even in excess of the layer thickness) but with a non-uniform melt depth. Balling is defined as an agglomeration of the particles, occurring when the liquid phase breaks up into a row of

Table 4 SEM images of the top view of PD1-LBP2 samples
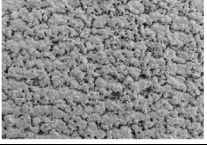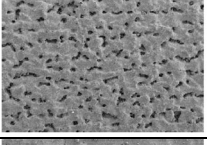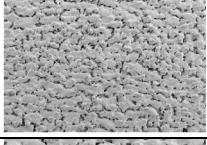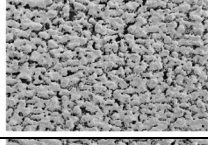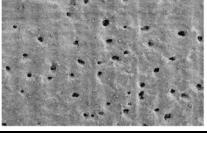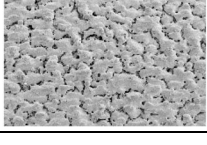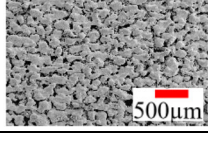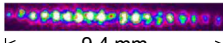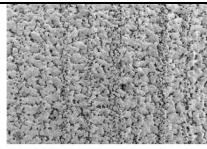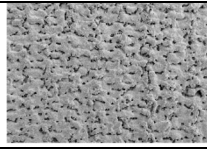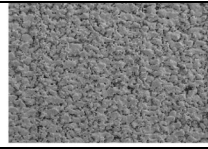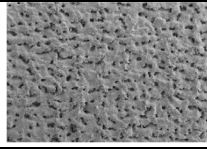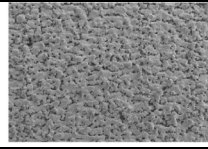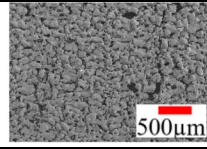
LBP2		
|← 6.5 mm →|		
Scan speed / **Laser power**	1 mm/s	3 mm/s	5 mm/s
30 W		Insufficient bonding	Insufficient bonding
40 W			
50 W			500μm

Table 5 SEM images of the top view of PD1-LBP3 samples

		LBP3	
		← 9.4 mm →	
	Scan speed		
Laser power	1 mm/s	3 mm/s	5 mm/s
30 W		Insufficient bonding	Insufficient bonding
40 W			Insufficient bonding
50 W			500μm

spheres to reduce surface energy [10]. The formation of balling as well as the weak bonding and partially melted particles led to interrupted melt tracks that promoted high porosities. Figure 7 shows plan-view SEM images of the top surface of two PD2 samples with different amounts of porosity.

Figure 7a depicts the melt defects observed during PD2 processing and Fig. 7b shows the melt disruption promoted by such defects when processing PD2 at the highest energy density. Melt disruptions can be observed along the scanning direction resulting in large amounts of porosity promoting

Table 6 SEM images of the top view of PD2-LBP1, PD2-LBP2 and PD2-LBP3 samples
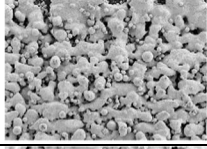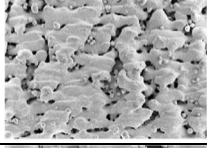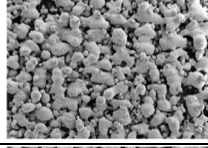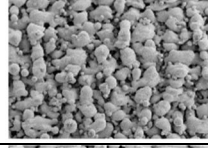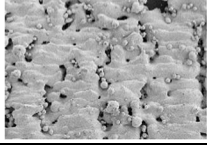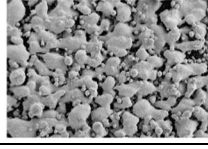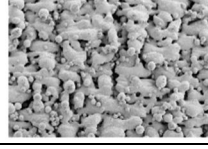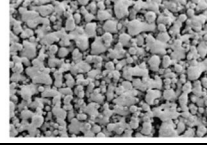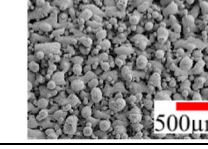
	PD2 – LBP1		PD2 – LBP2		PD2 – LBP3
	← 4.75 mm →		← 6.5 mm →		← 9.4 mm →
	Scan speed (mm/s)		**Scan speed (mm/s)**		**Scan speed (mm/s)**
Laser power	1	3	1	3	1
30 W		Insufficient bonding	Insufficient bonding	Insufficient bonding	Insufficient bonding
40 W				Insufficient bonding	Insufficient bonding
50 W					500μm

Fig. 5 **a** Emissivity and **b** conductivity of PD1 and PD2 powder beds for a range of temperatures. Calculated using the Sih and Barlow method
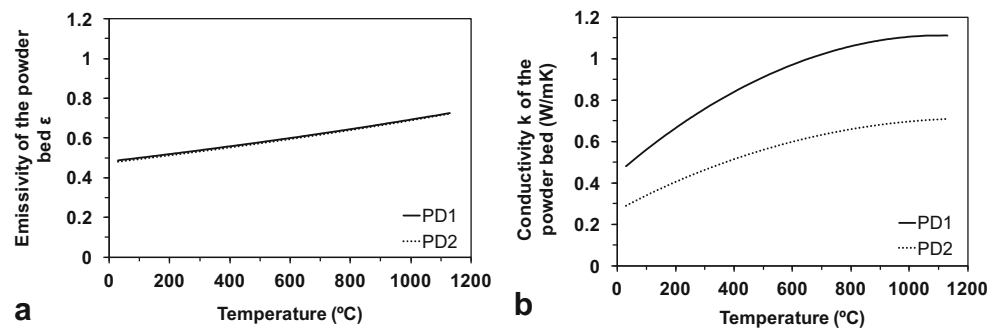
poor wettability even at the highest laser energy density. It has been observed, above, that the packing density (governed by the particle size distribution) of the powder bed has a strong influence on the melt stability and in determining porosity of a processed part. The characteristics of the powder determine physical variables, such as flowability of the melt and the nature of heat transfer as stated by Manakari et al. [10]. The densification behaviour can also be affected by powder defects such as satellites and inter-agglomerated pores that can cause lack of fusion between the particles. It can be assumed that such defects strongly influence the formation of melt instabilities and melt defects in the PD2 samples. It has been observed that smaller particle size distributions (such as PD1 here) tend to agglomerate during the melt, leading to stability of the melt whilst coarse particles (such as PD2) tend to segregate, leading to process instabilities [11]. Panels c and d of Fig. 7 show the corresponding PD1 samples produced at energy densities similar to those used for PD2 in Fig. 7a, b, respectively. PD1 surfaces do not show evidence of the melt defects observed with PD2, and very few pores are seen in Fig. 7d. The smaller particles of PD1 promote a homogeneous distribution of the powder bed increasing surface contact among the particles, which improves the heat transfer through the higher thermal conductivity. Smaller powder particle sizes used during SLM of stainless steel were also found to result in higher part densities across a wider range of process parameters (i.e. beam diameter, scan speed) than larger particle sizes, similar observations seen in work by Liu et al. [12]. Within this work, 22 out of 27 experimental trials on PD1 resulted in successful fusion, from which 8 displayed > 90% top surface density. In contrast, only 9 of the 27 PD2 samples were

successfully processed, from which only 3 were > 90% dense (a 60% reduction due to use of a coarser powder).

4.2 Effect of laser beam profile

Figure 8 plots the reduction of top surface porosity, (a), and the increasing melt depth, (b), in PD1 samples as a function of energy density for the different laser beam profiles LBP1, LBP2 and LBP3. All LBP1 treatments resulted in melted parts that could be removed from the powder bed (i.e. would not break-up when handled). Most of the LBP2 samples were also successfully melted. However, the LBP3 configuration resulted in more highly porous, partially melted samples. It can be seen in Fig. 8a that within the range of 10–20 J/mm^3 LBP1 showed less porosity compared with LBP2 and LBP3. This can be attributed to the continuous overlapping of laser spots creating a continuous melting area comprised by smaller melting spots. However, Ilie et al. [13] report that porosity in stainless steel samples can vary when varying laser power or scanning velocity at same energy densities due to lack of fusion, Rayleigh instability, balling or poor wetting characteristics as detailed by Rombouts et al. [14]. Decreasing levels of porosity were observed for LBP2 when scanned at 1 mm/s compared to the higher laser traversing speeds of 3 and 5 mm/s. This prevented any clear trend from appearing in the porosity data for LBP2 as shown in Fig. 8a. The porosity trends depicted in Fig. 8a generally indicate that the laser beam profile characteristics (i.e. beam diameter and spot spacing) affect the samples porosity. A melting array with smaller, more closely spaced spots presented a more efficient energy density distribution that resulted in denser parts being formed at similar

Table 7 Material properties for emissivity and conductivity calculations

Material	Fractional porosity φ_f	Particle size range (μm)	Solid density[a] (kg/m^3)	Bulk density[b] (kg/m^3)
PD1	0.47	15–45	7870	5298
PD2	0.48	44–106	7870	5279

[a] Density of the solid material

[b] Density of the powder bed

Fig. 6 **a** Top surface porosity and **b** melt depth in terms of energy density for PD1 and PD2 with their corresponding trendlines
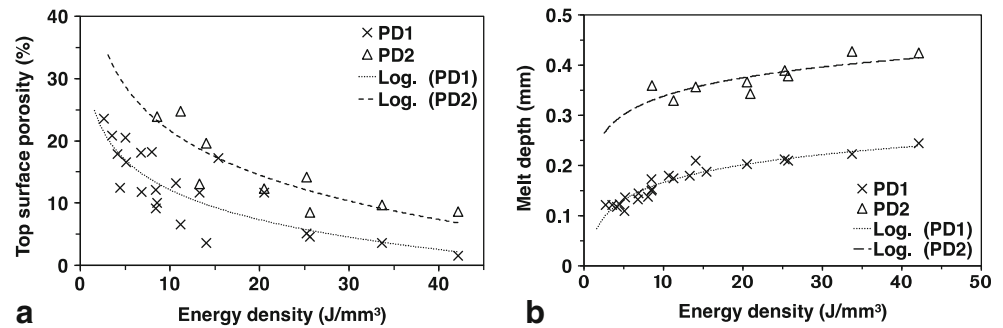
energy density compared to LBP2 and LBP3. Figure 8b demonstrates that LBP has no significant effect on the melt depth, which increases with energy density at a similar rate for the three LBPs. The spot spacing and the spot size have a negligible effect on the melt depth at the same energy densities.

Figure 9 shows the top view of samples produced at the same laser power and scanning speed for LBP3, (a), and LBP1, (b). The beam profiles are shown in the insets to these figures. The LBP3 sample in Fig. 9a exhibits visible areas of partial melting in between fully fused tracks along the scanning direction. The LBP1 sample in Fig. 9b showed no such evidence of partially melted areas. It is important to mention that the laser spot diameter of LBP3 is larger than that of LBP1, resulting in a lower beam power density for LBP3. However, it can be seen that the melt tracks (areas directly irradiated by the laser spots) in the LBP3 sample appear to be comparatively similar to the LBP1 sample, processed using the same parameters. A continuous melting beam distribution (stripe-shaped beam) therefore results in denser parts compared to a non-continuous beam distribution (multi-spot-shaped beam) at the same energy densities, as evidenced by the porosity trends in Fig. 8a.

4.3 Effect of laser power and scan speed

The effect of laser power and scan speed on the top surface porosity and melt depth is shown in Fig. 10 for particle size distribution PD1 for the three laser beam profiles LBP1, LBP2 and LBP3. In all cases, increasing laser power and/or decreasing scan speed results in a decrease in porosity and an increase in the melt depth. This is most evident for LBP1. It can be deduced from this study that higher sample densification (less porosity) can be achieved by increasing the input energy through increasing laser power and/or decreasing scanning velocity, as also described in work by Rombouts et al. [15].

For LPB1, the magnitude of the laser energy is increased through overlapping scan lines and use of tighter laser spots. Therefore, whilst the trends are also evident for LBP2 and LBP3, they are more pronounced for LBP1. It can be seen in Fig. 10a that the highest energy density treatment of LBP1 at 50 W and 1 mm/s resulted in near full top surface density whilst a melt depth close to the 260 μm layer thickness (244.3 μm) is achieved, Fig. 10b. It follows that even though top surface density approaches 100% for LBP1 (e.g. ~ 2% porosity at 1 mm/s, 50 W in Fig. 10a), the input energy may

Fig. 7 Plan-view SEM images of processed **a** and **b** PD2 and **c** and **d** PD1 at **a** and **c** 20.5 J/mm² and **b** and **d** 42 J/mm² energy density, respectively. Melt defects and melt disruptions generated high porosity in **a** and **b** PD2 samples. Such melt defects are not observed in **c** and **d** PD1 samples. PD1 promoted high densification at increasing energy densities
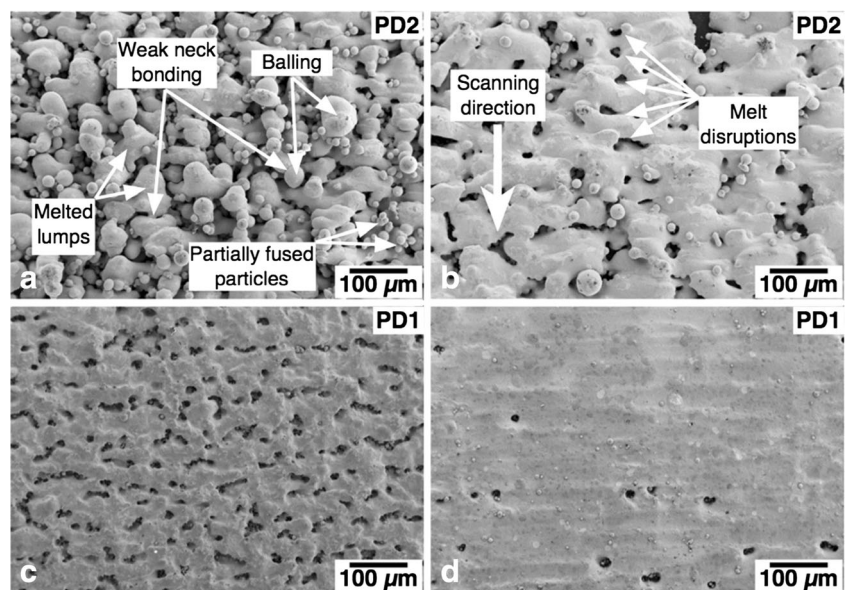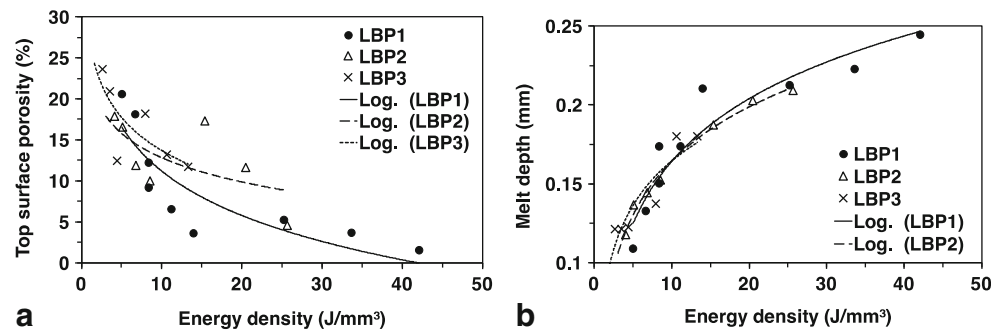
Fig. 8 Data measured and logarithmic trends of **a** top surface porosity and **b** melt depth as a function of energy density for the laser beam profiles LBP1, LBP2 and LBP3

still be insufficient to melt the full layer thickness, preventing successful bonding to the substrate. The high top surface porosity can be attributed to the stronger thermal conductivity in PD1 layers. The conductivity of powder is still low compared to that of solid material. Therefore, the laser-induced heat is retained in the powder, assisting the melt process. However, as the melt approaches the substrate, the higher conductivity of the substrate allows the heat to dissipate through the solid material preventing the melted powder from bonding to the substrate. It is anticipated that following the trends for LBP1 in Fig. 10a, b, a further increase of the laser power beyond 50 W would result in increased top surface density and a melt depth in excess of the layer thickness, which could enable bonding to the substrate. Figure 10a shows that the laser beam profile LBP1 produced the samples with the lowest top surface porosity at 1 and 3 mm/s scan speed. A clear trend of increasing melt depth and decreasing top surface porosity can be identified when increasing laser power at different scan speeds for LBP1. The top surface density, $\rho_{top\ surface}$, of the samples can be considered as $\rho_{top\ surface} = 1 - \varphi_{top\ surface}$, where $\varphi_{top\ surface}$ is the surface porosity. The degree of melt depth penetration within the powder bed can be described by the melt depth fraction δ where δ = melt depth/layer thickness. It has been observed that in all cases (or treatments) $\delta < \rho_{top\ surface}$. The quality of the melt can be described by the ratio $\delta/\rho_{top\ surface}$ where a fully melted layer thickness with full density is represented by $\delta/\rho_{top\ surface} = 1$. This is true only for trends of decreasing top surface porosity and increasing melt depth as shown in

Fig. 10a, b, respectively. Therefore, $\rho_{top\ surface} \rightarrow 1$ and $\delta \rightarrow 1$ are desirable indicators for a 'high quality melt'.

The ratio $\delta/\rho_{top\ surface}$ is plotted as a function of laser power and scanning velocity in Fig. 11a and as a function of energy density in Fig. 11b. The ratio $\delta/\rho_{top\ surface}$ increases with increasing laser power and reducing scan speed and therefore increases with increasing energy density. This behaviour suggests that during DAM of 316L stainless steel powder, the quality of the melt depends strongly on the scanning velocity. However, this limitation of scanning velocity can be compensated by the potential scalability of the total processing area, which can be increased as required (scale up the number of emitters) maintaining the energy density. This proportion can be increased further if the single-spot melting area is reduced and/or if the individual laser power is increased (as described in Section 3) resulting in a higher energy density. According to the trend shown in Fig. 11b, for a ratio $\delta/\rho_{top\ surface} > 1$, a theoretical energy density in excess of 55 J/mm³ would be required. This can be achieved by increasing power to 66 W or decreasing melting area to 0.91 mm² at 1 mm/s scan speed. It is suggested that under $\delta/\rho_{top\ surface} > 1$ conditions, bonding to the substrate will be achieved.

4.4 Cross-sectional density

Dense samples showing < 10% top surface porosity were obtained using LBP1 and scan speeds 1 and 3 mm/s at 30, 40 and 50 W. These samples were cross-sectioned and polished in order to measure the cross-sectional porosity at the macro $\varphi_{cross-macro}$ and micro $\varphi_{cross-micro}$ levels via optical

Fig. 9 Plan-view SEM images of the top surface of **a** LBP3 and **b** LBP1 samples processed at 30 W laser power and 1 mm/s scan speed with (a) non-continuous (individual multi-spots) and (b) continuous (line-shape) melt beam distribution. Beam profiles shown in the insets of figures for visualisation
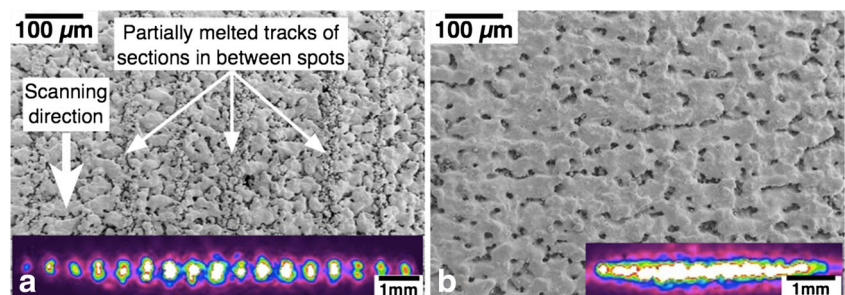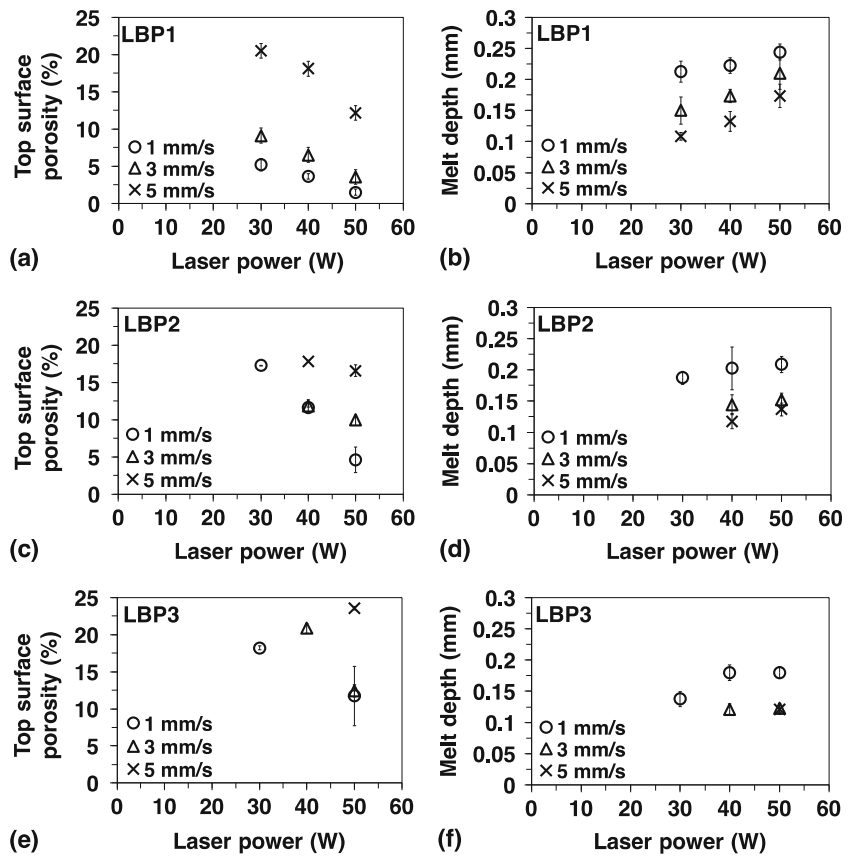
Fig. 10 Effect of laser power and scan speed on **a**, **c**, **d** top surface porosity and **b**, **d**, **f** melt depth for **a** and **b** LBP1, **c** and **d** LBP2 and **e** and **f** LBP3 for particle size distribution PD1


analysis. The density of the samples can be considered as $\rho_{\text{cross-macro}} = 1 - \varphi_{\text{cross-macro}}$ and $\rho_{\text{cross-micro}} = 1 - \varphi_{\text{cross-micro}}$ for the macro and micro levels, respectively. Figure 12 shows the macro and micro cross-sectional views of one of the selected samples. The $\rho_{\text{cross-macro}}$ was calculated by measuring the total cross-sectional area of a theoretical fully melted layer for the correspondent parameters and comparing it with the actual melted cross-sectional area (cross-sectional melt fraction with respect to a fully dense cross-section; see Fig. 12a).

Measurement of the cross-sectional melt area fraction visualised in Fig. 12a was compared to the total area within the yellow line that represents a theoretical fully dense cross-sectional area. This measurement was performed for all of the cross-sectioned samples. It should be noted that the

modulation depicted in the cross-sectional macro view (Fig. 12a) is a result of compressive stress from the hot mounting process, where molten Bakelite and clips were used to hold the thin single-layer samples in place. The boundary of the yellow line in Fig. 12 was defined taking into account the modulation caused by the compressing stress. The top boundary describes the sample's deformation and the bottom boundary connects the deeper points of the melted depths across the sample. The $\rho_{\text{cross-micro}}$ was obtained by measuring density values of several areas across the melt and calculating the mean density (see Fig. 12b).

In all cases, it was observed that $\rho_{\text{cross-micro}} > \rho_{\text{top surface}}$ and $\rho_{\text{cross-macro}} < \rho_{\text{top surface}}$. Therefore, the ratios $\rho_{\text{top surface}}/\rho_{\text{cross-micro}}$ and $\rho_{\text{cross-macro}}/\rho_{\text{top surface}}$ were used to describe the

Fig. 11 **a** Relation of the ratio $\delta/\rho_{\text{top surface}}$ to laser power and scanning velocity; **b** trend of the ratio $\delta/\rho_{\text{top surface}}$ with increasing energy density. Both for LBP1 and PD1
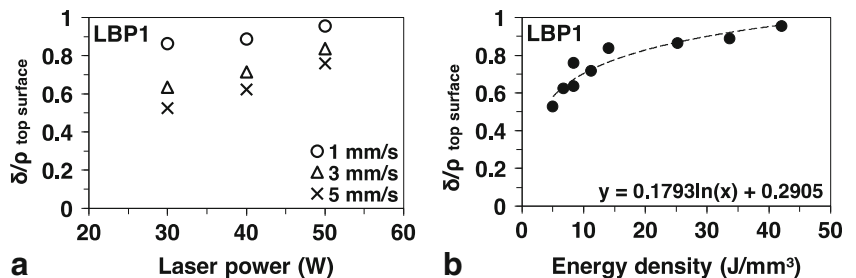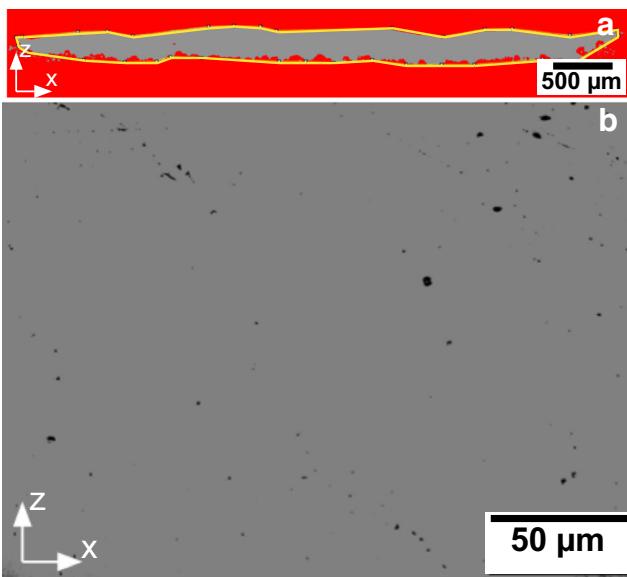
Fig. 12 a Cross-sectional macro view showing the melt fraction with respect to a fully dense single-layer cross-section (depicted by the thin yellow line) and **b** cross-sectional micro porosity of the LBP1 sample, both produced at 1 mm/s and 50 W

and $\rho_{cross-macro}$ densities and the values for the ratios $\rho_{top\,surface}/\rho_{cross-micro}$ and $\rho_{cross-macro}/\rho_{top\,surface}$ of the selected samples. It is assumed that as $\rho_{top\,surface}/\rho_{cross-micro} \rightarrow 1$ and $\rho_{cross-macro}/\rho_{top\,surface} \rightarrow 1$, micro and macro cross-sectional areas within a melt will tend towards full density, with a fully dense top surface.

Figure 13a, b plots the $\varphi_{cross-micro}$ and $\varphi_{cross-macro}$, respectively, as a function of both laser power and scanning velocity. Figure 13c, d plots the ratios $\rho_{top\,surface}/\rho_{cross-micro}$ and $\rho_{cross-macro}/\rho_{top\,surface}$ as a function of laser power and scanning velocity. Figure 13e, f plots these ratios as a function of energy density. It can be seen in Fig. 13a that most of the selected samples showed a ~ 0.2 $\varphi_{cross-micro}$ (99.8% density) similar to conventional 316L stainless steel SLM parts [13]. The slower 1 mm/s scan speed showed a stable trend of low $\varphi_{cross-micro}$ whilst the higher 3 mm/s scan speed showed a high rate of decreasing $\varphi_{cross-micro}$ from ~ 1.4 to ~ 0.2% at increasing laser power. Figure 13b shows a decreasing $\varphi_{cross-macro}$ with increasing laser power and decreasing scanning velocity. It is observed a steep decrease of $\varphi_{cross-macro}$ when processing at the slower 1 mm/s scan speed compared to a more stable $\varphi_{cross-macro}$ at 3 mm/s. Figure 13c depicts a clear increase of the ratio $\rho_{top\,surface}/\rho_{cross-micro}$ with increasing laser power and decreasing scanning velocity. Figure 13d shows a constant $\rho_{cross-macro}/\rho_{top\,surface}$ ratio at 3 mm/s scan speed and a high rate of increasing $\rho_{cross-macro}/\rho_{top\,surface}$ ratio at 1 mm/s scan

densification trend considering the decreasing tendency of $\varphi_{top\,surface}$ (or increasing tendency of $\rho_{top\,surface}$) with increasing energy density presented in Section 4.3. Figure 13 plots the measured $\varphi_{cross-micro}$ and $\varphi_{cross-macro}$ porosities, $\rho_{cross-micro}$

Fig. 13 a Cross-micro porosity at different laser power and scanning velocities; **b** cross-macro porosity at different laser power and scanning velocities; **c** ratio $\rho_{top\,surface}/\rho_{cross-micro}$ at different laser power and scanning velocities; **d** ratio $\rho_{cross-macro}/\rho_{top\,surface}$ at different laser power and scanning velocities; **e** ratio $\rho_{top\,surface}/\rho_{cross-micro}$ with energy density; **f** ratio $\rho_{cross-macro}/\rho_{top\,surface}$ with energy density
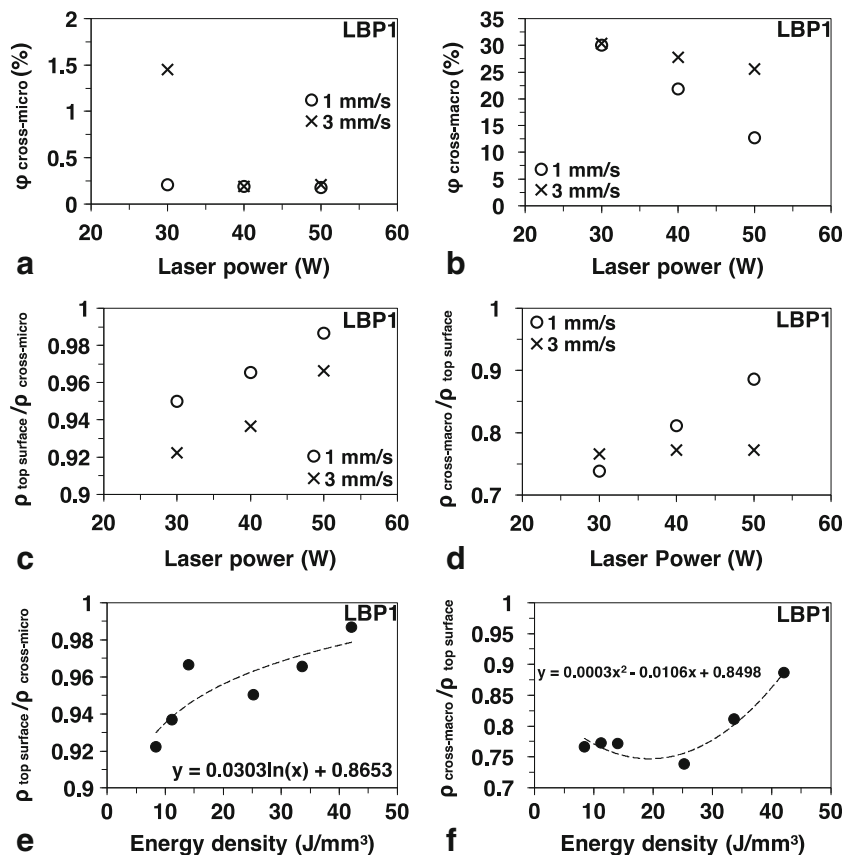
speed with increasing laser power. Figure 13e, f plots $\rho_{\text{top surface}}/\rho_{\text{cross-micro}}$ and $\rho_{\text{cross-macro}}/\rho_{\text{top surface}}$ as a function of energy density. The dashed lines in Fig. 13e, f represent fits to the data. According to these fits (equations provided in the figures), a theoretical minimum of 86 and 46.5 J/mm^3 energy density would be required in order to achieve full cross-micro and full cross-macro densities (resulting in $\rho_{\text{top surface}}/\rho_{\text{cross-micro}} = 1$ and $\rho_{\text{cross-macro}}/\rho_{\text{top surface}} = 1$), respectively. This suggests that the ratio of $\rho_{\text{top surface}}/\rho_{\text{cross-micro}}$ is the governing factor that identifies the minimum energy density required for processing fully dense parts. Energy densities in excess of 86 J/mm^3 could be achieved by optimising the beam delivery system and/or increasing laser power as described in Section 3.

5 Conclusion

It was observed that the packing density of the powder (which is in turn highly dependent on the particle size distribution) plays a crucial role in processing using the DAM method. The thermal conductivity of the powder bed, particle diameter and powder processing defects (i.e. satellites and inter-agglomeration pores) were identified as the main powder characteristics that limit DAM processing. Use of large powder particles resulted in low powder conductivity and correspondingly a 'low quality melt' that led to balling formation, weak particle bonding and partially fused particles. In contrast, smaller particle sizes of spherical shaped powder resulted in higher thermal conductivity leading to a 'higher quality melt'.

The effect of laser beam profiles during DAM has been analysed for a range of laser beam profiles from striped array to spatially separated spots. It has been identified that tight superposed melting spots with minimum spot spacing (i.e. a tight stripe-shape melting area comprised by multiple individual melting spots) present the optimal melting beam profile for a DAM process. A further reduction of individual melting spot area and spacing can be achieved by optimisation of the beam delivery system. The beam collimation mechanism (comprised by the FAC and SAC) can be identified as the governing factor in determining the minimum individual melting spot dimensions and the minimum spots period.

Finally, the influence of laser power and scanning velocity (i.e. energy density) on top surface density, cross-micro and cross-macro densities, and melt depth on powder have been investigated. It was found that increasing energy density resulted in denser parts and increased melt depth on powder. The ratios of melt depth fraction to top surface density $\delta/\rho_{\text{top surface}}$, top surface to cross-micro density $\rho_{\text{top surface}}/\rho_{\text{cross-micro}}$ and cross-macro to top surface density $\rho_{\text{cross-macro}}/\rho_{\text{top surface}}$ were introduced in order to identify the minimum energy density required to achieve theoretical full part density within the DAM process. A theoretical value of 86 J/mm^3 is suggested as the minimum energy density required for fully dense parts,

which can be attained through either increased power (to 103 W), slower scan speed (to 0.48 mm/s) (system then requiring water cooling) or decreased spot size to 120 μm diameter by using a different focal length FAC micro-optic.

References

1. Laskin A, Laskin V (2011) "Applying of refractive spatial beam shapers with scanning optics," Laser Institute of America Proc. ICALEO 2011, Paper M604
2. Miller D, Bucklew J, Enloe K, Plourde D, Lindahl B (2015) High density galvo housing for use with multiple laser beams; galvo system and laser beam processing system with such housing. Patent EP20140193417 Available at: http://www.google.com/patents/EP2902148A1. Accessed June 2017
3. Murr LE et al (2012) Fabrication of metal and alloy components by additive manufacturing: examples of 3D materials science. J Mater Res Technol 1:42–54
4. Li L (2000) Advances and characteristics of high-power diode laser materials processing. Opt. Lasers Eng. 34(4–6):231–253
5. Hengesbach S et al (2015a) Brightness and average power as driver for advancements in diode lasers and their applications. In: M. S. Zediker, ed. International Society for Optics and Photonics, p. 93480B (2015). Available at: http://proceedings.spiedigitallibrary.org/proceeding.aspx?doi=10.1117/12.2085068. Accessed June 2017
6. Hinke C, Merkt S, Eibl F, Schrage J, Bremen S (2015a) Additive manufacturing: perspectives for diode lasers. In 2015 IEEE High Power Diode Lasers and Systems Conference (HPD). IEEE. pp.39–40. Available at: http://ieeexplore.ieee.org/document/7439684/. Accessed June 2017
7. Matthews MJ et al (2017) Diode-based additive manufacturing of metals using an optically-addressable light valve. Opt Express 25(10):11788
8. Zavala-Arredondo M et al (2017) Laser diode area melting for high speed additive manufacturing of metallic components. Mater Des 117:305–315
9. Sumin Sih S, Barlow JW (2004) The prediction of the emissivity and thermal conductivity of powder beds. Part Sci Technol 22:427–440
10. Manakari V, Parande G, Gupta M (2016) Selective laser melting of magnesium and magnesium alloy powders: a review. Metals (Basel). 7(1):2
11. Simchi A (2004) The role of particle size on the laser sintering of iron powder. Metallurg and Mat Trans 35B
12. Liu B, Wildman R, Tuck C, Ashcroft I, Hague R (2011) "Investigation the effect of particle size distribution on processing parameters optimisation in selective laser melting process." Solid Freeform Fabrication Symposium. Austin, Texas

13. Ilie A, Ali H, Mumtaz K (2017) In-built customised mechanical failure of 316L components fabricated using selective laser melting. Technologies 5(1):9

14. Rombouts M, Kruth JP, Froyen L, Mercelis P (2006) Fundamentals of selective laser melting of alloyed steel powders. CIRP Ann - Manuf Technol 55(1):187–192

15. Simchi A, Pohl H (2003) Effects of laser sintering processing parameters on the microstructure and densification of iron powder. Mater Sci Eng A 359(1):119–128